Ultrasonic Heating Distribution in Lossy Cylinders and Spheres

LESTER A. LONGLEY AND WILLIAM D. O'BRIEN, JR., SENIOR MEMBER, IEEE

Abstract—The distribution of heat generation by viscous loss in infinitely long cylinders and spheres is estimated, based on the lossless acoustic wave distributions resulting from an incident plane wave. The characteristics of the objects are typical of tissue, while the lossless surrounding medium is similar to water. Impedance mismatches of up to 20 percent are considered for $1 < ka < 40$. Plots of typical heat generation distributions are presented, and apparent trends are summarized. The greatest spatial nonuniformity and highest peaks of heat generation were found for maximum ka and impedance mismatch.

I. Introduction

APPLICATIONS of ultrasound in medical diagnostics include fetal examination, diagnosis of cardiac problems, and blood flow measurements. However, it is known that sufficiently high acoustic intensity levels can destroy tissue, so that care must be exercised in ultrasonic irradiation. This paper examines the relatively high levels of localized heat generation that can result from the nonuniform wave distributions within irradiated tissues.

This issue has been addressed by Chan *et al.* [1], who determined the distribution and amount of heat generation in lossy tissue for the specific case of longitudinal and shear acoustic wave propagation through multiple plane layers. In particular, they verified that maximum heating occurs at the layer boundaries and determined that the heating depended on the layer thicknesses and acoustic property mismatches.

Love and Kremkau [2] calculated the intracellular temperature distribution of an ultrasonically irradiated biological cell. The cell was modeled as three concentric spheres with different thermal and acoustic properties, and the temperature distribution was obtained by solving the appropriate heat flow equations, assuming uniform absorption of acoustic energy within each region. The temperature changes—a maximum of 0.13 mK for an incident intensity of 1 W/cm^2—were found to be insignificant.

Kritikos and Schwan [3], [4] analyzed the similar problem of heat generation by electromagnetic waves (termed "heating potential") in conducting spheres of radii 5 and 10 cm. The latter sphere notably resembles a baby's head in both size and shape. For intermediate frequency ranges, maximum heating occurs near the center of the sphere and is otherwise found at the front boundary. A later paper [5] extends this work to include multilayered spheres, which correspond even more closely to a baby's head. The most recent work of Kritikos and Schwan [6] analyzes the effects of heat conduction and of heat convection by means of blood flow in this spherical geometry.

The work reported herein [7] is specifically concerned with heat generation in tissue from acoustic absorption. Although this is only one factor in the tissue temperature distribution, it is thought that sites of maximum heat generation by this mechanism would give a reasonable indication of tissue "hot spots." To determine the temperature distribution accurately would require consideration of heat generation by metabolic processes in addition to ultrasonic absorption. Also, heat removal by blood flow and heat conduction within the tissue would have to be included.

The acoustic wave energy loss is analyzed for two object shapes: an infinitely long cylinder and a sphere. It is assumed that each object has a uniform lossy interior similar to tissue, and that it is surrounded by an infinite lossless material with different acoustical properties similar to water. The loss occurring in the interior of each object has been calculated for the situation of an incident plane wave originating an infinite distance away from the object. These calculations were made for various object sizes and acoustic impedance mismatches in order to elicit general trends in the locations and relative magnitudes of hot spots.

The cylinder and sphere were chosen for examination partly for geometrical simplicity and also because of biological relevance. Many vessels, tubes, axons, and fibers can be modeled as cylinders. Also, certain cell masses, such as glands, small tumors, and young fetuses are approximately spherical. All calculations were performed on a Cyber 175, using programs written in Fortran Extended, Version 4.

II. Calculation of Pressure Distribution

The first step in determining loss is the calculation of the steady-state pressure distribution inside a *lossless* cylinder or sphere in the presence of the source wave. From these calculations, estimates for absorptive heat generation in *lossy*—but otherwise identical to the lossless—objects are obtained using a method which assumes a bulk-viscosity loss mechanism. No

Manuscript received September 1, 1981. This work was partially supported by U.S. Food and Drug Administration Grant FD 927 and by the National Science Foundation for the NSF Graduate Fellowship (L. A. Longley).

L. A. Longley was with the Bioacoustics Research Laboratory, Department of Electrical Engineering, University of Illinois, Urbana, IL. He is now with Motorola, Inc., Room 2928, 1301 E. Algonquin Rd., Schaumburg, IL 60196.

W. D. O'Brien, Jr. is with the Bioacoustics Research Laboratory, Department of Electrical Engineering, University of Illinois, 1406 W. Green St., Urbana, IL 61801.

0018-9537/82/0300-0069$00.75

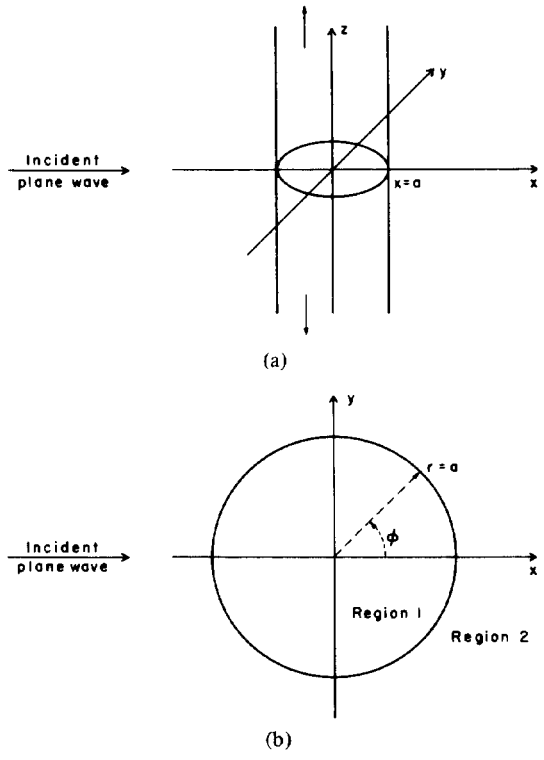

Fig. 1. Geometry of cylinder problem. (a) Cylinder of radius a and of infinite extent in the z coordinate. (b) Cross section of cylinder, for arbitrary z.

perturbation of the lossless distributions was attempted to refine these estimates.

The calculation of acoustic wave spatial distributions under lossless conditions is based on the "first-order" wave equations:

$$\frac{\partial p}{\partial t} = -\rho c^2 (\overline{\nabla} \cdot \vec{u}) \tag{1a}$$

and

$$\rho \frac{\partial \vec{u}}{\partial t} = -\overline{\nabla} p. \tag{1b}$$

These equations are stated in terms of two wave variables: the scalar pressure (p) and the particle velocity vector ($\vec{u}$); and two material parameters: the acoustic velocity (c) and the density (ρ).

The use of the scalar-variable pressure instead of the stress tensor follows from the assumption that all particle motion is longitudinal, so that no shear wave is present. Actually, some shear wave component does exist near tissue boundaries, where it is created by mode conversion. Its relatively high attenuation in tissue results in a surface region of heating, but the overall effect is low, owing to the relatively low conversion in tissue of energy from an incident longitudinal wave to a reflected or transmitted shear wave [8].

A. Cylinder

First, it is desired to find the acoustic wave distribution resulting when a source plane wave is incident on a "soft" (fluid-like) cylinder, as shown in Fig. 1. The pressure *within* the cylinder (region 1) is denoted in complex form by $\boldsymbol{p}_w$, while the pressure outside (region 2) is given by $\boldsymbol{p}_s + \boldsymbol{p}_i$. The symbol $\boldsymbol{p}_s$ represents the *scattered* component, and $\boldsymbol{p}_i$ is the known *incident* plane wave.

The wave solution is found by combining the coupled wave equations (1), in terms of two variables, into a single second-order equation with a single variable (p). This equation is solved by the method of separation of variables, resulting in a general solution containing a sinusoidal time factor, a radial factor in terms of cylindrical Bessel functions, and a sinusoidal angular factor. Thus, the expression for $\boldsymbol{p}_w$ is of the form

$$\boldsymbol{p}_w(r, \phi, t) = \left[\sum_{m=0}^{\infty} \boldsymbol{W}_m J_m(k_1 r) \cos(m\phi) \right] \cdot \exp(-i\omega t), \quad 0 \leqslant r \leqslant a \tag{2}$$

where k_1 is the object wavenumber, ω is the incident wave frequency, $\boldsymbol{W}_m$ is the mth complex weighting amplitude, J_m is the cylindrical Bessel function of the first kind of order m, and a is the cylinder radius.

The boundary conditions, requiring continuity of pressure ($\boldsymbol{p}$) and of the normal (i.e., radial) component of particle velocity ($\boldsymbol{u}_r$) at the cylinder boundary ($r = a$), are used to obtain expressions for $\boldsymbol{W}_m$. The final results for $m = 0$ are

$$\boldsymbol{W}_0 = \frac{P}{\boldsymbol{\Delta}_0} [\boldsymbol{H}_1(k_2 a) J_0(k_2 a) - \boldsymbol{H}_0(k_2 a) J_1(k_2 a)] \tag{3}$$

where

$$\boldsymbol{\Delta}_0 = \boldsymbol{H}_1(k_2 a) J_0(k_1 a) - \boldsymbol{H}_0(k_2 a) J_1(k_1 a) \cdot Z_r \tag{4}$$

where P is the incident wave amplitude, $\boldsymbol{H}_m$ is the cylindrical Hankel function of the first kind of order m, and

$$Z_r = \frac{Z_2}{Z_1}. \tag{5}$$

The quantities

$$Z_1 = \rho_1 c_1 \tag{6a}$$

and

$$Z_2 = \rho_2 c_2 \tag{6b}$$

are the characteristic acoustic impedances. The corresponding expression for $m > 0$ is

$$\boldsymbol{W}_m = \frac{2Pi^m}{\boldsymbol{\Delta}_m} \{ [\boldsymbol{H}_{m+1}(k_2 a) - \boldsymbol{H}_{m-1}(k_2 a)] J_m(k_2 a) - \boldsymbol{H}_m(k_2 a) [J_{m+1}(k_2 a) - J_{m-1}(k_2 a)] \} \tag{7}$$

where

$$\boldsymbol{\Delta}_m = [\boldsymbol{H}_{m+1}(k_2 a) - \boldsymbol{H}_{m-1}(k_2 a)] J_m(k_1 a) - \boldsymbol{H}_m(k_2 a) [J_{m+1}(k_1 a) - J_{m-1}(k_1 a)] \cdot Z_r. \tag{8}$$

B. Sphere

The spherical case (Fig. 2) uses similar notation and a similar approach as in the cylindrical case. The pressure within the

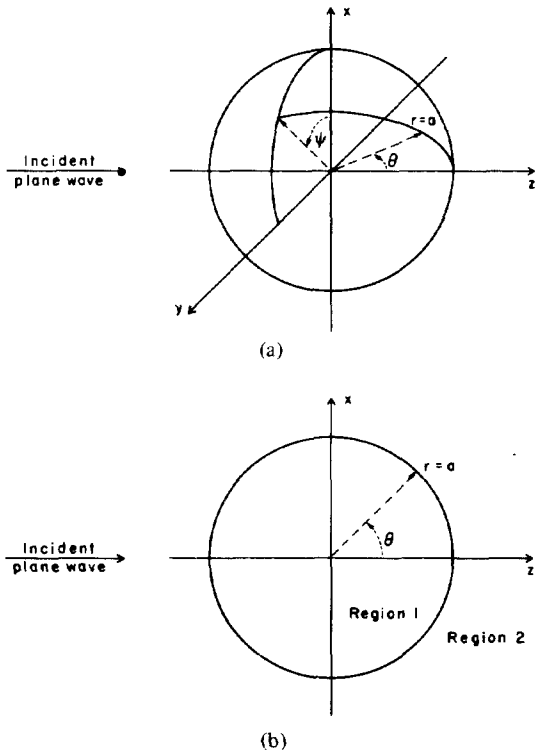

Fig. 2. Geometry of sphere problem. (a) Sphere of radius a. (b) Cross section of sphere for $\psi = 0$.

sphere ($\boldsymbol{p}_w$) takes the form

$$\boldsymbol{p}_w(r,\theta,t) = \left[\sum_{m=0}^{\infty} \boldsymbol{W}_m j_m(k_1 r) P_m(\cos\theta)\right] \cdot \exp(-i\omega t), \quad 0 \leqslant r \leqslant a \tag{9}$$

where j_m is the spherical Bessel function of the first kind and $P_m(\cos\theta)$ is the Legendre polynomial, both of order m, a is the radius of the sphere, and the remaining quantities assume the same definitions as in the cylindrical case.

The general solution for $m \geqslant 0$ is

$$\boldsymbol{W}_m = \frac{(2m+1)Pi^m}{\boldsymbol{\Delta}_m}\{[(m+1)\boldsymbol{h}_{m+1}(k_2 a) - m\boldsymbol{h}_{m-1}(k_2 a)]\, j_m(k_2 a) - \boldsymbol{h}_m(k_2 a) \cdot [(m+1) j_{m+1}(k_2 a) - m j_{m-1}(k_2 a)]\} \tag{10}$$

where

$$\boldsymbol{\Delta}_m = [(m+1)\boldsymbol{h}_{m+1}(k_2 a) - m\boldsymbol{h}_{m-1}(k_2 a)]\, j_m(k_1 a) - \boldsymbol{h}_m(k_2 a)[(m+1) j_{m+1}(k_1 a) - m j_{m-1}(k_1 a)] \cdot Z_r \tag{11}$$

and $\boldsymbol{h}_m$ is the spherical Hankel function of the first kind of order m.

III. Estimation of Heat Generation

The distribution of wave energy absorbed by the tissue is estimated using the previous pressure distributions. It is assumed that the material parameters (acoustic velocity, density, etc.) are constant over the range of temperatures experienced by the irradiated tissue, and that the wave distribution (pressure and particle velocity) is not altered by the conversion of wave energy to heat in the tissue.

At least two mechanisms of energy absorption are known for soft tissues: viscous loss and heat conduction. In tissues, viscous losses are much greater than those owing to heat conduction, so that the former mechanism is considered to be the sole source of heating, and the wave is assumed to propagate adiabatically.

A theoretical analysis of the viscous loss problem is presented by Morse and Ingard [9]. The following relation, taken directly from that development, expresses the instantaneous (i.e., not time-averaged) power loss per unit volume (D) in terms of instantaneous real pressure and velocity:

$$D = \left[\eta + \frac{4}{3}\mu\right](\bar{\nabla}\cdot\vec{u})^2 + \mu|\bar{\nabla}\times\vec{u}|^2 - 4\mu\left[\frac{\partial u_x}{\partial x}\frac{\partial u_y}{\partial y} + \frac{\partial u_x}{\partial x}\frac{\partial u_z}{\partial z} + \frac{\partial u_y}{\partial y}\frac{\partial u_z}{\partial z} - \frac{\partial u_x}{\partial y}\frac{\partial u_y}{\partial x} - \frac{\partial u_x}{\partial z}\frac{\partial u_z}{\partial x} - \frac{\partial u_y}{\partial z}\frac{\partial u_z}{\partial y}\right] \tag{12}$$

where η is the bulk viscosity coefficient, and μ is the shear viscosity coefficient. This equation is derived for gases, but its relative simplicity motivates this attempted application for tissues.

The constant μ is assumed to have the same value for tissues as for water, namely $\mu = 10^{-6}$ mg/mm · μs. In contrast, η for tissues is generally on the order of 10^{-3} mg/mm · μs. Therefore, for $\mu \ll \eta$, and also assuming that the magnitudes of the other factors are not markedly different, (12) simplifies to

$$D \cong \eta(\bar{\nabla}\cdot\vec{u})^2. \tag{13}$$

This equation can be restated in a more useful form by re-expressing the divergence term using (1a):

$$\bar{\nabla}\cdot\vec{u} = \mathrm{Re}(\bar{\nabla}\cdot\vec{\boldsymbol{u}}) = \mathrm{Re}\left\{\left[\frac{ik}{Z}\right]\boldsymbol{p}\right\} = \frac{k}{Z}|\boldsymbol{p}'|\sin(\omega t - \measuredangle\,\boldsymbol{p}') \tag{14}$$

where $|\boldsymbol{p}'|$ and $\measuredangle\,\boldsymbol{p}'$ denote the magnitude and phase, respectively, of $\boldsymbol{p}'$, the time-independent part of $\boldsymbol{p}$.

The time-averaged power loss ($\langle D\rangle$) is obtained from (13) and (14):

$$\langle D\rangle \cong \frac{\eta}{2}\left[\frac{k|\boldsymbol{p}'|}{Z}\right]^2 \tag{15}$$

where k and Z are known constants, and $\boldsymbol{p}'$ for this lossy case is approximated by the previously evaluated lossless pressure distribution.

The bulk viscosity coefficient is determined by turning to the simpler case of loss in plane wave propagation. For this case, the experimentally measured total power loss per unit volume ($\langle dQ\rangle$), given in terms of the known absorption co-

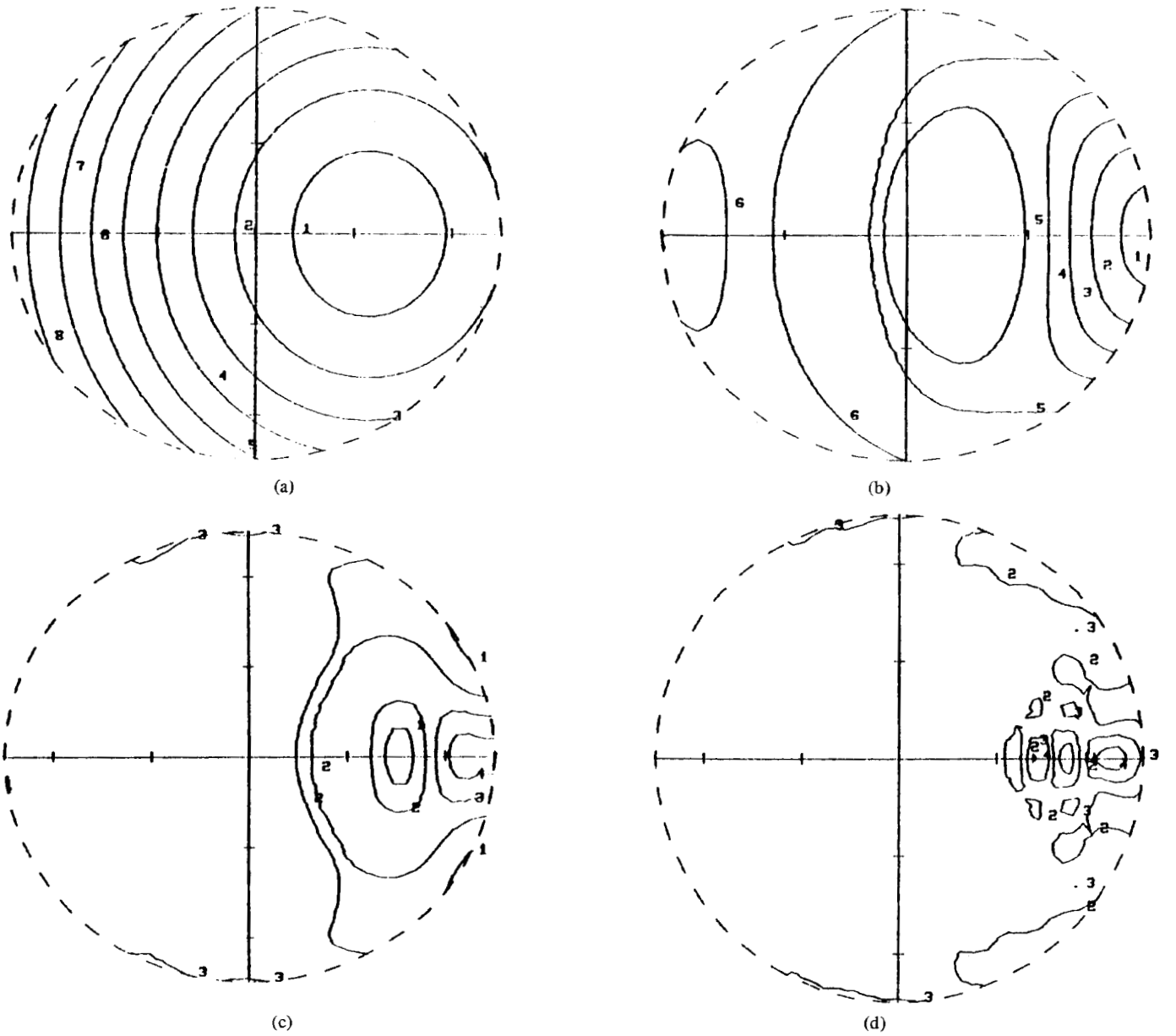

Fig. 3. Dependence of heat generation ($\langle D_1 \rangle$) in sphere on radius (a), shown for a 5 percent velocity mismatch ($c_1 = 1.05 \times c_2, \rho_1 = \rho_2$). Incident plane wave originates infinitely far left of sphere. See Table I for values of $\langle D_1 \rangle$ on contours. (a) $a = 0.25$ mm, $k_1 a = 1$. (b) $a = 1$ mm, $k_1 a = 4$. (c) $a = 2.5$ mm, $k_1 a = 10$. (d) $a = 5$ mm, $k_1 a = 20$.

efficient α, is equated with viscous power loss ($\langle D \rangle$), in terms of η, so that η can be expressed in terms of α. This step assumes that a bulk viscosity mechanism is entirely responsible for power loss of the acoustic wave in the tissue. Now, power loss in terms of α is

$$\langle dQ \rangle = \alpha \cdot \frac{|\boldsymbol{p}'|^2}{Z}. \tag{16}$$

When $\langle dQ \rangle$ and $\langle D \rangle$ are equated, the following relation is readily derived:

$$\eta = \frac{2\alpha Z}{k^2}. \tag{17}$$

Finally, (15) and (17) are combined to form a simple estimate for viscous loss in the object interior:

$$\langle D_1 \rangle = \frac{\alpha_1 |\boldsymbol{p}'_w|^2}{Z_1}. \tag{18}$$

IV. Computational Results

The values of computational parameters were chosen with regard to ultrasonic irradiation of tissue in medical situations. In particular, to examine the relationship between object size and acoustic wavelength, the radius of the object was varied over the range 0.25-10 mm, with frequency constant, so that $k_1 a$ took on values from about 1-40. The former extreme approaches the long wavelength limit ($\lambda_1 >> a$) with $\lambda_1 \sim 6a$, whereas the latter extreme nears the short wavelength limit ($\lambda_1 << a$) with $\lambda_1 \sim a/6$. For these cases, a 5 percent velocity-only impedance mismatch ($c_1 = 1.05 \times c_2$, $\rho_1 = \rho_2$) was used.

To explore the effects of impedance mismatches, the values of ρ_1 and c_1 were individually varied by ±5 percent and ±20 percent with respect to ρ_2 and c_2. The smaller range represents typical tissue variations, while the larger corresponds with maximum observed variations. For these cases, the value

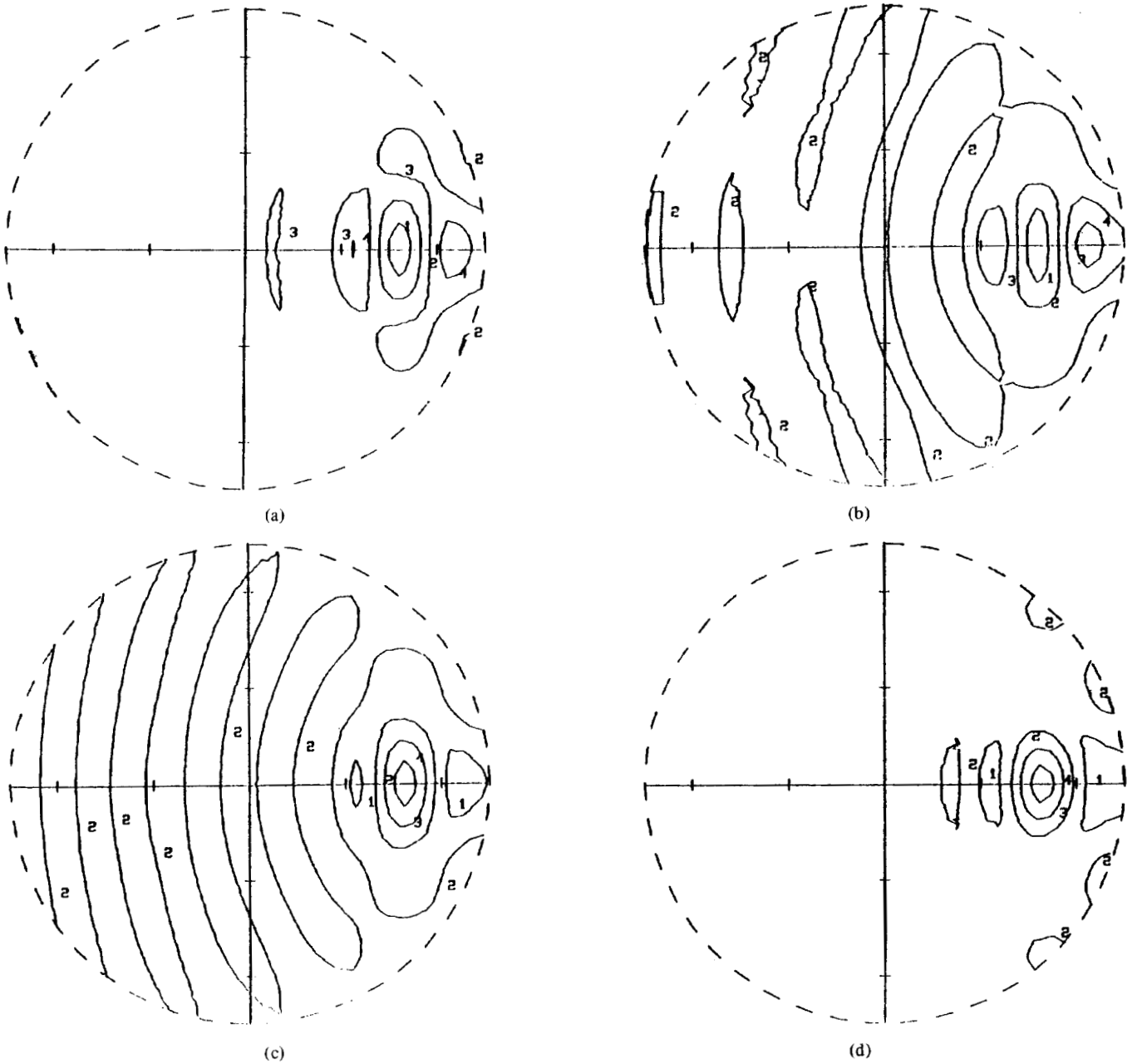

Fig. 4. Dependence of heat generation ($\langle D_1 \rangle$) in sphere on the density mismatch, shown for $\rho_1 \pm 5$ percent and $\pm$ 20 percent with respect to ρ_2 and $k_1 a = 10.5$ ($a = 2.5$ mm, $c_1 = c_2$). Incident plane wave originates infinitely far left of sphere. See Table II for values of $\langle D_1 \rangle$ on contours. (a) $\rho_1 = 1.05 \times \rho_2$. (b) $\rho_1 = 1.2 \times \rho_2$. (c) $\rho_1 = 0.95 \times \rho_2$. (d) $\rho_1 = 0.8 \times \rho_2$.

$a = 2.5$ mm was used, so that the interior wavenumber had an intermediate value $k_1 a \cong 10$.

The remaining parameters were set to the same values for all cases considered. In particular, the frequency of the incident wave is always $f = 1$ MHz. The absorption coefficient is $\alpha_1 = 0.005$ Np/mm, a typical value for tissues with low collagen content, at $f = 1$ MHz. Also, for the lossless surrounding medium in region 2, the values $\rho_2 = 1$ mg/mm^3 and $c_2 = 1.5$ mm/μs were used; these values, near those of water at 20°C, are also characteristic of soft, fluid-like tissue [10], [11]. The normalizing value $P = 1$ N/mm^2 for the incident pressure amplitude was chosen to remove P, in effect, from the various expressions.

The first three sets of plots, Figs. 3-5, show the distribution of viscous loss ($\langle D_1 \rangle$) in a sphere for four values each of a, ρ_1, and c_1, respectively. The trends illustrated for the sphere are generally true of the cylinder also, although spatial nonuniformity and maximum values of heat generation tend to be more extreme for the sphere. Selected cases are repeated for the cylinder in Fig. 6, to illustrate the similarity to and notable differences with the spherical cases.

In these plots, the distribution of estimated heat generation within the cylinder or sphere is represented by numbered contours within a dashed circle indicating the object boundary. The heating level numbers, displayed just to the right of a randomly chosen point on each contour, are keyed to values of $\langle D_1 \rangle$ by means of Tables I-IV. The contours are constructed by means of linear interpolation between calculated values on a grid of 20 (radial) $\times$ 100 (angular) equally spaced points. It should be noted that interpolation near the center

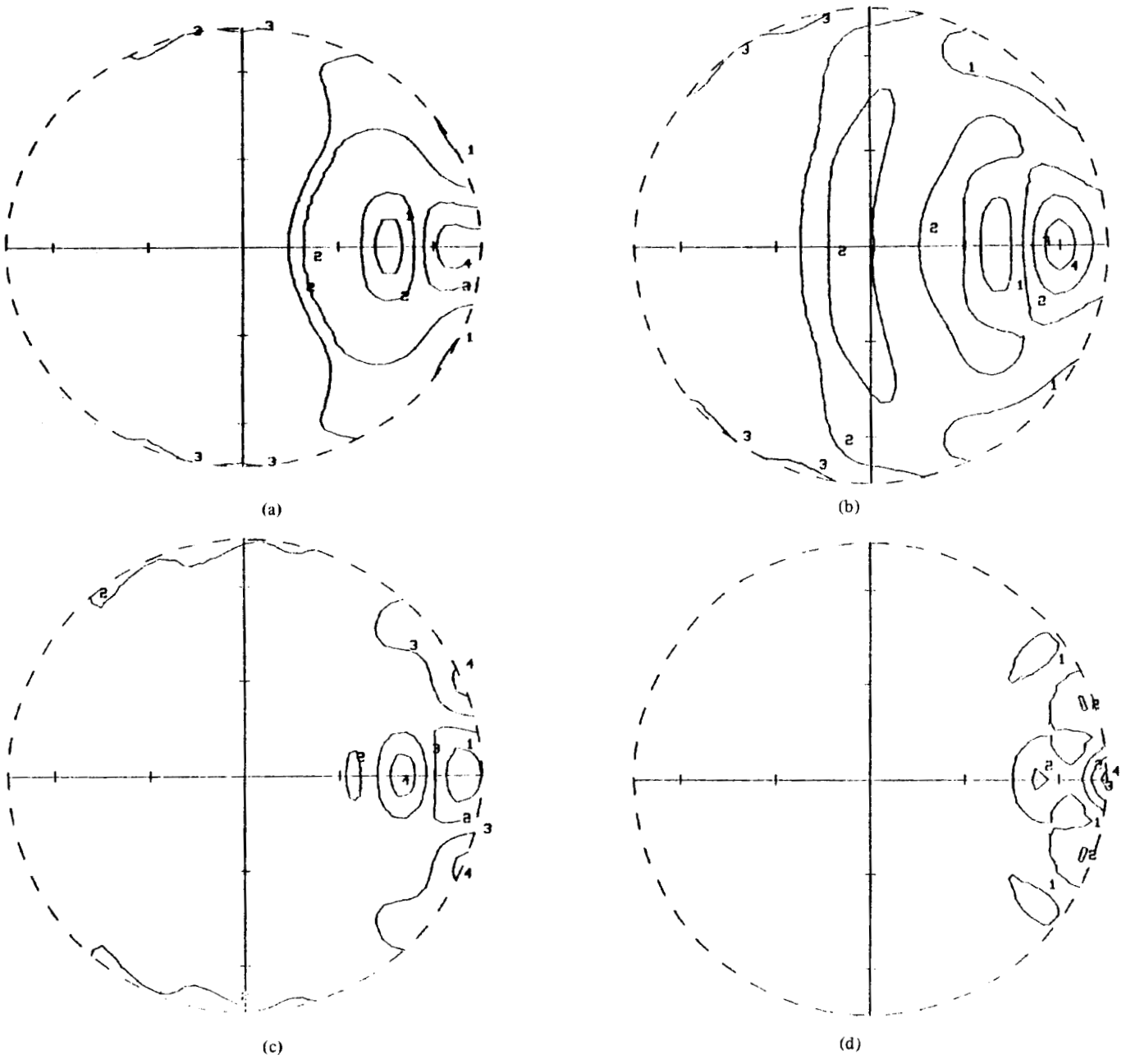

Fig. 5. Dependence of heat generation ($\langle D_1 \rangle$) in sphere on the velocity mismatch, shown for c_1 ± 5 percent and ± 20 percent with respect to c_2 and $k_1 a \simeq 10$ (a = 2.5 mm, $\rho_1 = \rho_2$). Incident plane wave originates infinitely far left of sphere. See Table III values of $\langle D_1 \rangle$ on contours. (a) $c_1 = 1.05 \times c_2, k_1 a = 10.0$. (b) $c_1 = 1.2 \times c_2, k_1 a = 8.7$. (c) $c_1 = 0.95 \times c_2, k_1 a = 11.0$. (d) $c_1 = 0.8 \times c_2, k_1 a = 13.1$.

point is relatively poor and produces some anomalous results, which are readily identifiable and should be ignored.

In Fig. 3, it is seen that for spheres of smaller radii, more heating occurs at the "upstream" (left) boundary. For spheres of larger radii, the heat generation is spatially more diverse, including hot spots with a "focused" appearance inside the "downstream" (right) half.

Higher spatial "peakedness" is also seen in Fig. 4 to occur for larger density mismatches. For these cases, using an intermediate value $k_1 a \simeq 10$, the hottest spots are observed in the interior of the downstream half of the spheres. Also, note the standing wave pattern in Fig. 4(c), indicated by the prominent "bands" in the upstream portion of the sphere.

Fig. 5 shows more spatial "peakedness" for larger velocity mismatches, especially for $c_1 < c_2$. Again for $k_1 a \simeq 10$, the hot spots are observed in the downstream half of the spheres, both in the interior and at the boundary.

Figs. 6(a) and 3(b), showing a cylinder and sphere, respectively, of identical radius and acoustic properties, exemplify the similarity in distributions of heat generation which often occurs with the two object shapes. In contrast, Figs. 6(b) and 3(d) illustrate the difference in distributions which also can occur. In this case, standing waves are apparent only with the cylinder, and the sites of maximum heat generation differ noticeably. The presence of standing waves in the cylinder is the main difference observed between Figs. 6(c) and 4(a).

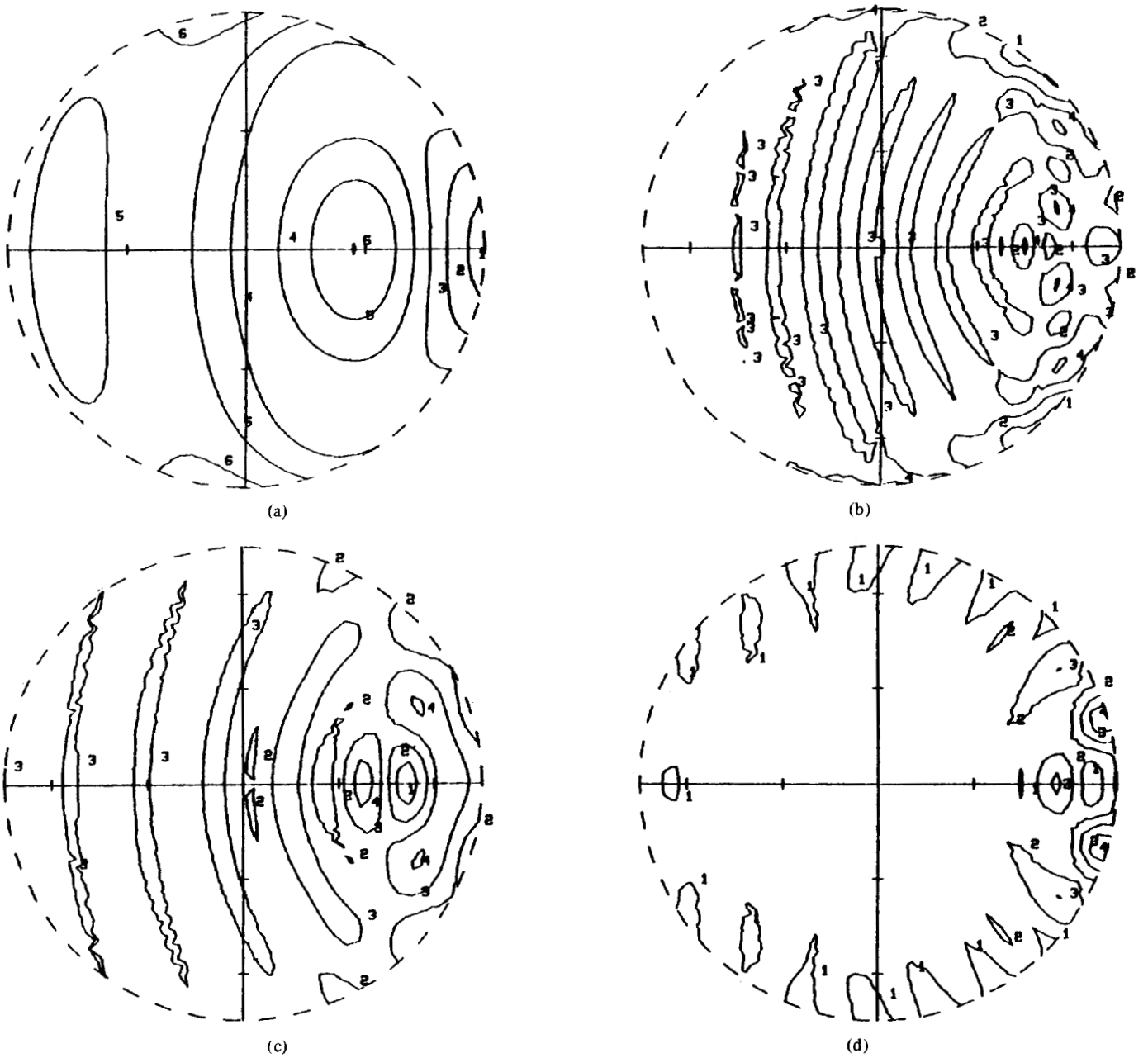

Fig. 6. Assorted cases of heat generation ($\langle D_1 \rangle$) in cylinder. Incident plane wave originates infinitely far left of cylinder. See Table IV for values of $\langle D_1 \rangle$ on contours. (a) $a = 1$ mm, $\rho_1 = \rho_2, c_1 = 1.05 \times c_2, k_1 a = 4.00$. (b) $a = 5$ mm, $\rho_1 = \rho_2$, $c_1 = 1.05 \times c_2, k_1 a = 19.9$. (c) $a = 2.5$ mm, $\rho_1 = 1.05 \times \rho_2, c_1 = c_2, k_1 a = 10.5$. (d) $a = 2.5$ mm, $\rho_1 = \rho_2, c_1 = 0.8 \times c_2, k_1 a = 13.1$.

TABLE I
HEAT GENERATION CROSS REFERENCE FOR FIG. 3

Heating Level Number	Corresponding Value of $\langle D_1 \rangle$ (mW/mm^3)			
	Fig. 3(a)	Fig. 3(b)	Fig. 3(c)	Fig. 3(d)
1	2.94	1.72	2.03	1.52
2	2.97	2.03	2.77	2.58
3	3.01	2.33	3.51	3.64
4	3.05	2.64	4.25	4.69
5	3.08	2.95		
6	3.12	3.26		
7	3.15			
8	3.19			

Finally, the locations of hot spots and the shapes of the distributions are again seen to differ somewhat between Figs. 6(d) and 5(d). In spite of these frequent differences between the cylinder and the sphere, the distributions are mostly similar, and the generalizations made about the sphere are also true for the cylinder, although the most extreme cases usually occur with the sphere.

Tables V-VII list the *maximum* estimated heat generation (within each object) for several values of a, ρ_1, and c_1, respectively, for both the cylinder and the sphere. These tabulations include all cases in Figs. 3-6 and some additional cases without plotted distributions. These numbers should be compared to

TABLE II
HEAT GENERATION CROSS REFERENCE FOR FIG. 4

Heating Level Number	Corresponding Value of $\langle D_1 \rangle$ (mW/mm^3)			
	Fig. 4(a)	Fig. 4(b)	Fig. 4(c)	Fig. 4(d)
1	2.50	1.31	2.78	1.92
2	3.00	3.09	3.34	4.52
3	3.51	4.87	3.89	7.12
4	4.01	6.65	4.44	9.72

TABLE III
HEAT GENERATION CROSS REFERENCE FOR FIG. 5

Heating Level Number	Corresponding Value of $\langle D_1 \rangle$ (mW/mm^3)			
	Fig. 5(a)	Fig. 5(b)	Fig. 5(c)	Fig. 5(d)
1	2.03	0.99	1.73	12.91
2	2.77	2.33	3.20	38.63
3	3.51	3.68	4.67	64.35
4	4.25	5.03	6.14	90.07

TABLE IV
HEAT GENERATION CROSS REFERENCE FOR FIG. 6

Heating Level Number	Corresponding Value of $\langle D_1 \rangle$ (mW/mm^3)			
	Fig. 6(a)	Fig. 6(b)	Fig. 6(c)	Fig. 6(d)
1	2.51	2.12	2.95	2.39
2	2.70	2.66	3.18	6.94
3	2.88	3.20	3.41	11.50
4	3.07	3.74	3.64	16.06
5	3.25			
6	3.44			

TABLE V
DEPENDENCE OF MAXIMUM HEAT GENERATION (MAXIMUM $\langle D_1 \rangle$) IN CYLINDER AND SPHERE ON RADIUS (a) FOR A 5 PERCENT VELOCITY MISMATCH
($c_1 = 1.05 \times c_2$, $\rho_1 = \rho_2$)

a (mm)	Maximum $\langle D_1 \rangle$ (mW/mm^3)	
	In Cylinder	In Sphere
0.25	3.3	3.2
0.5	3.4	3.3
1.0	3.5	3.4
2.5	3.7	4.6
5.0	4.0	5.2
10.0	4.4	7.6

TABLE VI
DEPENDENCE OF MAXIMUM HEAT GENERATION (MAXIMUM $\langle D_1 \rangle$) IN CYLINDER AND SPHERE ON DENSITY MISMATCH FOR $k_1 a \sim 10$
($a = 2.5$ mm, $c_1 = c_2$)

Density Ratio (ρ_1/ρ_2)	Maximum $\langle D_1 \rangle$ (mW/mm^3)	
	In Cylinder	In Sphere
0.8	6.1	11.0
0.95	3.9	4.7
1.05	3.8	4.3
1.2	5.0	7.5

TABLE VII
DEPENDENCE OF MAXIMUM HEAT GENERATION (MAXIMUM $\langle D_1 \rangle$) IN CYLINDER AND SPHERE ON VELOCITY MISMATCH FOR $k_1 a \sim 10$
($a = 2.5$ mm, $\rho_1 = \rho_2$)

Velocity Ratio (c_1/c_2)	Maximum $\langle D_1 \rangle$ (mW/mm^3)	
	In Cylinder	In Sphere
0.8	18.3	103.0
0.95	5.0	6.9
1.05	3.7	4.6
1.2	4.5	5.7

a base value of 3.3 mW/mm^3, representing the *uniform* heat generation that would occur with no mismatch ($\rho_1 = \rho_2$, $c_1 = c_2$) for objects of any size and shape. In fact, these values have only relative meaning in comparison to the base value, because all have been obtained using an arbitrary value for the incident wave amplitude, namely $P = 1$ N/mm^2.

It is readily seen in Table V that maximum $\langle D_1 \rangle$ increases steadily with increasing radius a for both the cylinder and the sphere. For smaller objects of both shapes, a rather smooth viscous-loss distribution is indicated by maximum $\langle D_1 \rangle$ being approximately equal to the "base" (i.e., no mismatch) value 3.3 mW/mm^3. However, the maximum $\langle D_1 \rangle$ increases to 130 percent of this value for the largest cylinder and to 220 percent for the largest sphere.

Table VI indicates that maximum heat generation is larger for greater density mismatches for $\rho_1 > \rho_2$ and somewhat more so for $\rho_1 < \rho_2$. The most extreme cases for the cylinder and the sphere both occur for $\rho_1 = 0.8 \times \rho_2$, for which the maximum $\langle D_1 \rangle$ is 180 percent and 330 percent, respectively, of the base value.

Table VII shows a similar trend with the velocity mismatch as that which occurs with the density mismatch, but the particular values are much more extreme for $c_1 < c_2$. In particular, for $c_1 = 0.8 \times c_2$, maximum heat generation in the cylinder is 550 percent higher than the base value, and in the sphere a peak of almost 3100 percent of this value is observed.

V. COMPUTATIONAL VERIFICATION

The Fortran programs calculating the pressure distributions for the soft cylinder and sphere were checked for several special cases. First, it was verified that the boundary conditions (namely, continuity of pressure and radial velocity at $r = a$) are satisfied. Second, it was determined that under conditions of no mismatch the calculated pressure is indeed uniform inside and outside the objects, with no scattered component. Finally, the soft object distributions were examined in the limiting rigid object case, for which the elasticity $\kappa_1 \equiv 1/\rho_1 c_1^2 \ll \kappa_2$. The scattered wave distribution for the soft object problem was in good agreement with that calculated using published rigid object solutions [9].

Furthermore, the rigid object programs using the aforementioned published solutions were themselves checked. In particular, calculated plots of the angular distribution of the far-field scattered radial intensity for $ka = 1$, 3, and 5 are compared with those published in [9]. As shown in Figs. 7 and 8, for the cylinder and sphere, respectively, the distributions

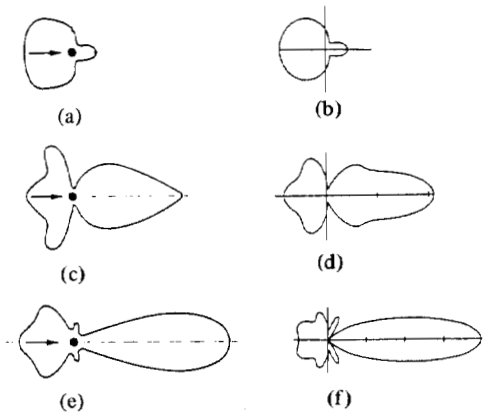

Fig. 7. A comparison of plots (b), (d), (f) prepared by the authors with pictures (a), (c), (e) published in [9, Fig. 8], both showing angular distribution of far-field scattered radial intensity for a rigid cylinder in the path of a plane wave moving to the right. The radius of intensity evaluation is $r = 100 \cdot a$ for the calculated plots, but is unknown for the published plots. (a), (b) $ka = 1$. (c), (d) $ka = 3$. (e), (f) $ka = 5$.

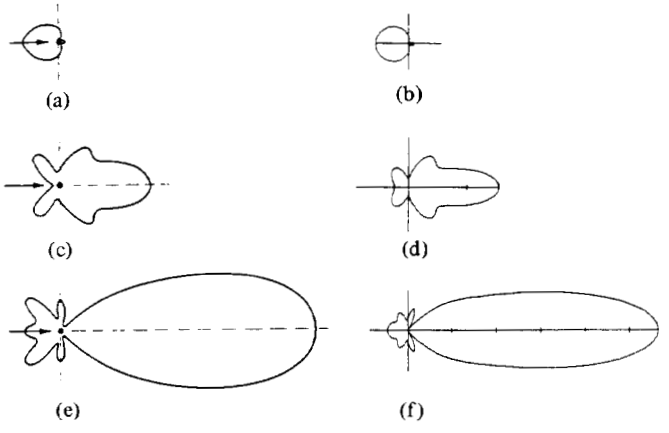

Fig. 8. A comparison of calculated (b), (d), (f) and published (a), (c), (e) plots of scattered intensity as in Fig. 7, but for a rigid sphere in this case. Again, the radius used for the calculated plots is $r = 100 \cdot a$, while that of the published plots is not known. (a), (b) $ka = 1$. (c), (d) $ka = 3$. (e), (f) $ka = 5$.

have very similar shapes. However, the visible discrepancies are attributed to inaccuracies in the plots, which were published in [12]. Such early calculations, made without the aid of a computer, undoubtedly required more gross approximations than needed with current techniques.

Finally, the mathematical subroutines used to calculate the various Bessel functions and the Legendre polynomials were, in some cases, checked prior to their release as "packaged programs," or else checked against published tables.

VI. Discussion and Conclusion

In conclusion, Figs. 3-6 have shown typical distributions of heat generation in the cylinder and sphere. The usual location of hot spots is at the upstream boundary of smaller objects and in the interior of larger objects or at the boundary of the downstream half. Also, the distributions tend to be more nonuniform for higher values of maximum heat generation. Tables V-VII have indicated several trends in the dependence of maximum heating on parameter values and object shape. Generally, larger objects and larger impedance mismatches contribute to greater local extremes in heating; this is particularly true for velocity mismatches where $c_1 < c_2$. Also, maximum heating is usually more extreme with the sphere, *ceteris paribus*; this consistent finding probably owes to the sphere being circular in all cross sections and thus better suited for "focusing," as compared with the single circular cross section of the cylinder. As can be predicted from these trends, the highest observed peak of heat generation—more than 30 times higher than the uniform heating with no mismatch—occurs for a sphere with a large velocity mismatch, with $c_1 < c_2$. This sphere is of an intermediate size ($k_1 a = 13.1$), and even higher peaks would be expected for larger spheres.

It is useful to compare the previous plots of the estimated viscous loss distribution in spheres with published illustrations of loss in spheres owing to electromagnetic (microwave) radiation [4]. For lower values of $k_1 a$, both types of energy result in quite similar solutions, with maximum heating at the upstream boundary. For higher values of $k_1 a$, for which the distributions are less uniform, some agreement is still seen: Maximum heating occurs in the downstream half of each sphere in both cases. However, the "focused" hot spots of electromagnetic origin are located nearer to the center of the sphere. It should be noted that this comparison is complicated by the two distinct "*E*-" and "*H*-plane" cross sections of the sphere resulting from the polarized incident electromagnetic wave, though the heating in these planes is usually similar.

Nomenclature

a	Cylinder radius and sphere radius.
c	Acoustic velocity.
c_1	Acoustic velocity in the object interior.
c_2	Acoustic velocity in the surrounding medium.
D	Instantaneous viscous power loss per unit volume.
$\langle D \rangle$	Time averaged value of D.
$\langle D_1 \rangle$	$\langle D \rangle$ in the object interior.
f	Frequency (Hz).
$\boldsymbol{h}_m(x)$	Spherical Hankel function of the first kind of order m and argument x.
$\boldsymbol{H}_m(x)$	Cylindrical Hankel function of the first kind of order m and argument x.
i	Complex number $\sqrt{-1}$.
$j_m(x)$	Spherical Bessel function of the first kind of order m and argument x.
$J_m(x)$	Cylindrical Bessel function of the first kind of order m and argument x.
k	Wavenumber.
k_1, k_2	Wavenumber in media 1 and 2, respectively.
$k_1 a$	Normalized dimension of the object in units of radians.
p	Acoustic pressure (scalar).
$\boldsymbol{p}$	Acoustic pressure (complex representation).
$\boldsymbol{p}'$	Time-independent part of $\boldsymbol{p}$.
$\boldsymbol{p}_i$	Acoustic pressure incident upon object.
$\boldsymbol{p}_s$	Acoustic pressure scattered component.
$\boldsymbol{p}_w$	Acoustic pressure within the object.
$\boldsymbol{p}'_w$	Time-independent part of $\boldsymbol{p}_w$.

P	Incident wave amplitude.
$P_m(x)$	Legendre polynomial of order m and argument x.
$\langle dQ \rangle$	Total power loss per unit volume.
$\vec{u}$	Particle velocity (vector).
$\vec{u}$	Particle velocity (complex representation).
u_r	Normal component of particle velocity (complex representation).
W_m	mth complex weighting amplitude for both the cylindrical and spherical cases.
Z	Characteristic acoustic impedance.
Z_1, Z_2	Characteristic acoustic impedance of media 1 and 2, respectively.
Z_r	Ratio of Z_1 to Z_2.
α	Absorption coefficient.
α_1	Absorption coefficient in the object interior.
η	Bulk viscosity coefficient.
κ_1, κ_2	Elasticity in media 1 and 2, respectively.
λ_1	Acoustic wavelength in the object interior.
μ	Shear viscosity coefficient.
ρ	Medium density.
ρ_1, ρ_2	Density in media 1 and 2, respectively.
ω	Angular frequency.
$\vec{\nabla}$	The del operator.

APPENDIX

The authors have recently learned of a paper [13] which contains an alternative derivation of the pressure-squared dependence of absorptive loss, confirming the relationship stated in (18). This result is applicable for arbitrary pressure distributions in materials with bulk viscosity but negligible shear viscosity.

REFERENCES

[1] A. K. Chan, R. A. Sigelmann, and A. W. Guy, "Calculations of therapeutic heat generated by ultrasound in fat-muscle-bone layers," *IEEE Trans. Biomed. Eng.*, vol. BME-21, no. 4, pp. 280–284, July 1974.

[2] L. A. Love and F. W. Kremkau, "Intracellular temperature distribution produced by ultrasound," *J. Acoust. Soc. Am.*, vol. 67, no. 3, pp. 1045–1050, Mar. 1980.

[3] H. N. Kritikos and H. P. Schwan, "Hot spots generated in conducting spheres by electromagnetic waves and biological implications," *IEEE Trans. Biomed. Eng.*, vol. BME-19, no. 1, pp. 53–58, Jan. 1972.

[4] —, "The distribution of heating potential inside lossy spheres," *IEEE Trans. Biomed. Eng.*, vol. BME-22, no. 6, pp. 457–463, Nov. 1975.

[5] —, "Formation of hot spots in multilayer spheres," *IEEE Trans. Biomed. Eng.*, vol. BME-23, no. 2, pp. 168–172, Mar. 1976.

[6] —, "Potential temperature rise induced by electromagnetic field in brain tissues," *IEEE Trans. Biomed. Eng.*, vol. BME-26, no. 1, pp. 29–33, Jan. 1979.

[7] L. A. Longley, "The distribution of ultrasonic heating in lossy cylinders and spheres," M.S. thesis, Dep. of Electrical Engineering, Univ. Illinois at Urbana–Champaign, 1980.

[8] L. A. Frizzell, "Ultrasonic heating of tissues," Unpublished Doctor's dissertation, Dep. of Electrical Engineering, Univ. Rochester, 1975, pp. 88–99.

[9] P. M. Morse and K. U. Ingard, *Theoretical Acoustics*. New York: McGraw-Hill, 1968.

[10] W. D. O'Brien, Jr., "The relationship between collagen and ultrasonic attenuation and velocity in tissue," in *Proc. 1977 Ultrason. Int. Conf.* Surrey, England: IPC Business Press, 1977, pp. 194–204.

[11] S. A. Goss, R. L. Johnston, and F. Dunn, "Comprehensive compilation of empirical ultrasonic properties of mammalian tissues," *J. Acoust. Soc. Am.*, vol. 64, no. 2, pp. 423–457, Aug. 1978.

[12] P. M. Morse, *Vibration and Sound*, 1st ed. New York: McGraw-Hill, 1936.

[13] W. L. Nyborg, "Heat generation by ultrasound in a relaxing medium," *J. Acoust. Soc. Am.*, vol. 70, no. 2, pp. 310–312, Aug. 1981.

Resolution Enhancement of Ultrasonic *B*-Scan Images by Deconvolution

WOLFGANG VOLLMANN

Abstract—**The measured signal in ultrasonic *B*-scan techniques may be considered as the convolution of a reflection coefficient, describing the object, with a point-spread function describing the shape of the ultrasonic pulse. Thus, one may try to enhance the resolution of *B*-scan images by deconvolution. How the resolution enhancement R depends on the signal-to-noise ratio (SNR) of the measured data is analyzed. A one-dimensional lateral deconvolution using a specified cutoff in the spatial frequency domain and a Gaussian point-spread function yields $R = \sqrt{\ln \text{SNR}}$. For SNR = 50 this formula predicts $R = 2$. Other point-spread functions yield other relations between R and SNR. The theoretical results are in agreement with experimental findings reported in the literature.**

Manuscript received June 17, 1981.

The author is with Philips GmbH Forschungslaboratorium Hamburg, D-2000 Hamburg 54, West Germany.

I. INTRODUCTION

ULTRASONIC imaging techniques are widely applied in medical diagnostics [1]. Most of these techniques are based on the *B*-scan principle [2], a pulse-echo method. A typical variant of the *B*-scan technique uses a single well-

0018-9537/82/0300-0078$00.75